

Ferroelectric 2D Antimony Oxides with Wide Bandgaps

Romakanta Bhattarai^a, Kai Ni^b, and Xiao Shen^{a*}

^aDepartment of Physics and Materials Science, The University of Memphis, Memphis, TN, USA

^bDepartment of Electrical and Microelectronic Engineering, Rochester Institute of Technology, Rochester, NY, USA

Abstract

The first two-dimensional (2D) polymorphs of antimony dioxide, namely, γ -Sb₂O₄ and δ -Sb₂O₄, are predicted using the evolutionary algorithm combined with first-principles density functional theory (DFT) calculations. Out-of-plane ferroelectricity is found in γ -Sb₂O₄, while in-plane ferroelectricity is found in δ -Sb₂O₄. The predicted dipole moment of γ -Sb₂O₄ and δ -Sb₂O₄ phases are 36.63 and 14.96 eÅ, respectively, implying that they can be good candidates for making ferroelectric devices. The calculations show that doping with other group V elements or applying strain can lower the switching energy barriers and thus facilitate switching. Results from GW calculations show indirect band gaps of 5.51 and 3.39 eV for γ -Sb₂O₄ and δ -Sb₂O₄ in their monolayers, respectively. Raman spectra are calculated to facilitate the experimental investigation of the predicted structures. The existence of both in-plane and out-of-plane 2D ferroelectricity and the large band gaps make this material system particularly interesting for potential applications.

Introduction

Ferroelectricity arises from a switchable spontaneous electric polarization in materials and is an intriguing feature in a wide range of materials. Ferroelectric materials have many potential applications, such as nonvolatile memory devices including ferroelectric capacitors and ferroelectric field effect transistor, and sensors.^{1,2} One major challenge in using these materials in miniature devices is the depolarization field developed as the material's thickness decreases, which often destroys the ferroelectricity by inhibiting the electric polarization.^{3,4} The two-dimensional (2D) van der Waals materials, however, offer an alternative path to overcome this problem, as recent findings of ferroelectric 2D materials make it possible to shrink the thicknesses of the ferroelectric devices down to atomic layers.⁵⁻⁹ 2D ferroelectrics include CuCl,¹⁰ MX (M=Sn,Ge;X=S,Se),¹¹ SnTe,⁷ In₂Se₃,^{6,12} As₂X₃ (X=S, Se, Te),^{6,13} WTe₂,⁹ CuInP₂S₆,⁸ some of which are also realized in the experiment.^{6-9,12,14,15} However, most of them show the in-plane electric polarization, which limits their applications in practical devices. The out-of-plane ferroelectricity, typically more desirable for nonvolatile memory applications, is extremely rare in 2D materials.^{8,9,12} More importantly, a large bandgap

* xshen1@memphis.edu

is desirable for applications as it enables a large voltage being applied and low leakage current, but most 2D ferroelectrics known so far have small bandgaps. Under these circumstances, the Sb-O system is particularly interesting because of its rich structures, possibility to possess large band gaps, and interesting dielectric properties.¹⁶⁻¹⁸

Several phases of antimony oxides have been investigated experimentally or theoretically. Among them, the α and β phases of Sb_2O_3 and Sb_2O_4 are the most studied. They are semiconductors with direct and indirect band gaps and smaller effective masses of the carriers.¹⁹⁻²³ These compounds have several applications ranging from catalysis to polymerization to coating.²⁴⁻²⁹ Zhang et al. investigated a number of layered antimonene oxides theoretically and found their band gaps ranging from 0 to 2.28 eV, along with $18\text{Sb}-18\text{O}$ as a topological insulator.³⁰ Theoretical investigation on other 2D Sb_2O_x ($x=1, 2, 3$) was reported by Wolff et al.¹⁶ Recently, Yang et al. reported experimental observation of new antimony oxide, $\text{SbO}_{1.93}$, in ultrathin samples, with an unusually large band gap (~ 6.3 eV) and a large static dielectric constant (~ 100).¹⁸ Interestingly, antimony selenide (SbSe) has long been known as a quasi-one-dimensional ferroelectric semiconductor,^{31,32} which suggests the potential of ferroelectricity in low-dimensional Sb compounds.

In this paper, we propose two new layered phases of the antimony oxide, named $\gamma\text{-Sb}_2\text{O}_4$, and $\delta\text{-Sb}_2\text{O}_4$, from the evolutionary algorithm combined with the first-principles calculations. Out-of-plane ferroelectricity is predicted in $\gamma\text{-Sb}_2\text{O}_4$, while in-plane ferroelectricity is predicted in $\delta\text{-Sb}_2\text{O}_4$. We also show that the doping and strain can be used to adjust the switching energy barrier. The large dipole moment of $\gamma\text{-Sb}_2\text{O}_4$ and $\delta\text{-Sb}_2\text{O}_4$ imply that they can be good candidates for ferroelectric applications. Their monolayers feature large band gaps. The Raman properties are also predicted. The results highlight the rich structures and properties of the Sb-O system. The finding of out-of-plane and in-plane 2D ferroelectric oxides with large bandgaps are important for potential applications of the 2D ferroelectrics.

Results

We used a genetic algorithm in combination with the density functional theory (DFT) to search for the stable structures corresponding to the local energy minimum. Details of the computational methods can be found in Supplementary Information, Section I. A total of 13130 structures are generated from the genetic algorithm with varying unit sizes, stoichiometry, and dimensionality. Among them, we obtain a total of three stable phases of Sb_2O_4 . One of them is the known $\alpha\text{-Sb}_2\text{O}_4$, whose appearance validates our methodology. The other two phases of Sb_2O_4 have not been reported previously, and we name them γ - and $\delta\text{-Sb}_2\text{O}_4$. It is interesting that these new phases, which are the first 2D antimony oxides with the stoichiometric ratio of 2:4, are found by the genetic algorithm in both the 3D and 2D searches. Figure 1

shows the crystal structures of the predicted phases. For δ - Sb_2O_4 , we explored the ABAB and ABBA types of stackings and found that the energy of ABAB stacking is lowered by 0.02 eV/atom. Therefore, we only focus on ABAB type of stackings, as shown in Fig. 1(c, d).

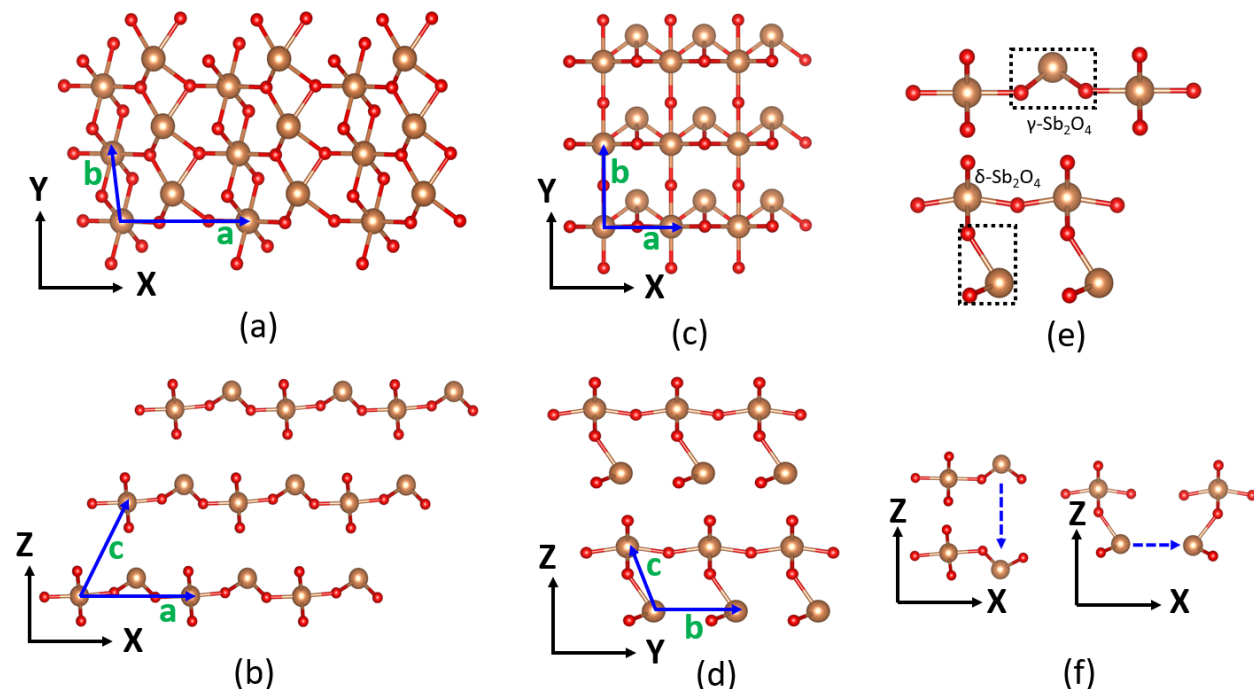


Table 1: Optimized lattice parameters of the γ - Sb_2O_4 , δ - Sb_2O_4 , and ε - Sb_2O_4

Phase	a (Å)	b (Å)	c (Å)	α (°)	β (°)	γ (°)	Volume (Å ³)	Bravais Lattice
γ - Sb_2O_4 (bulk)	6.55	3.06	5.87	75.4	61.4	90.2	99.09	Triclinic
γ - Sb_2O_4 (monolayer)	6.50	3.05	-	90	90	90	-	Rectangular
δ - Sb_2O_4 (bulk)	3.18	3.88	6.99	102.8	90	90	84.38	Triclinic
δ - Sb_2O_4 (monolayer)	3.16	3.88	-	90	90	90	-	Rectangular

First, we examine the bonding configurations in these Sb_2O_4 phases. In γ - Sb_2O_4 , two types of covalent bonding between antimony and oxygen atoms are observed, as clearly shown in Fig. 1(a). Type one consists of an Sb atom bonded octahedrally (6-fold) with six neighboring oxygen atoms, whereas in type two, each Sb atom is tetrahedrally (4-fold) bonded to four oxygen atoms. Four among the six oxygen atoms around the octahedrally bonded Sb are two-fold coordinated, connecting only with the octahedral Sb atoms. On the other hand, all the four oxygens around the tetrahedrally bonded Sb are three-fold coordinated, with two bonds connecting to tetrahedrally bonded Sb atoms and the third bond connecting to octahedrally bonded Sb atoms. In δ - Sb_2O_4 , a slight modification in bonding between Sb and O is observed. As shown in Fig. 1(b), one type of Sb is octahedrally (6-fold) bonded with six oxygen atoms as in the previous case, whereas

the other Sb atom is bonded to only three oxygen atoms (3-fold). The oxygen atoms have two-fold and three-fold covalent bonds with Sb, similar to the case of γ - Sb_2O_4 . Interestingly, in δ - Sb_2O_4 , the two types of Sb-O bonds are in two different planes within a single layer, while in γ - Sb_2O_4 , the two bonding types appear alternately along one direction within the same plane (Figure 1(e)). A detailed analysis of bonding environments among the γ - and δ - Sb_2O_4 phases and their corresponding bond lengths are presented in Supplementary Material, Section III.

These new layered Sb_2O_4 phases exhibit interesting ferroelectric properties, as the 4-fold and 3-fold Sb in γ - and δ - Sb_2O_4 are associated with electric dipoles switchable by an external electric field. As a result of their corresponding crystal structures, the γ - Sb_2O_4 phase exhibits an out-of-plane ferroelectric switching, and the δ - Sb_2O_4 phase exhibits an in-plane dipole switching (Fig. 1(f)). The calculated switching barriers for bulk phases of γ - and δ - Sb_2O_4 are shown in Figure 2. The maximum switching energy barrier for the dipole in γ - Sb_2O_4 is found to be 0.51 eV (Figure 2(a)), whereas, for δ - Sb_2O_4 , it is 0.43 eV (Figure 2(b)). We also explore the feasibility of reducing the energy barrier through doping at the Sb site. It is found that the barrier is lowered to 0.44 eV upon doping of Bi in γ - Sb_2O_4 , while it is decreased to 0.29 eV upon doping of As in δ - Sb_2O_4 . These values are comparable to the switching barriers in AlN and 2D In_2Se_3 ^{33,12}, and smaller than GaFeO_3 .³⁴ We also investigate the effect of strain in the γ - Sb_2O_4 phase by applying a tensile strain of +3% along the ‘a’ & ‘b’ axis and -3% along the ‘c’ axis. The energy barrier is decreased by 0.13 eV to 0.38 eV, suggesting that the strain can be another method to decrease the switching barrier in the γ - Sb_2O_4 . The electric dipole moment in γ - Sb_2O_4 is 36.63 eÅ per unit cell in the out-of-plane direction, whereas in δ - Sb_2O_4 , the moment is 14.96 eÅ per unit cell along the in-plane direction. These values are comparable with the croconic acid and GaFeO_3 ,^{34,35} and imply that they can be good candidates for ferroelectric applications.

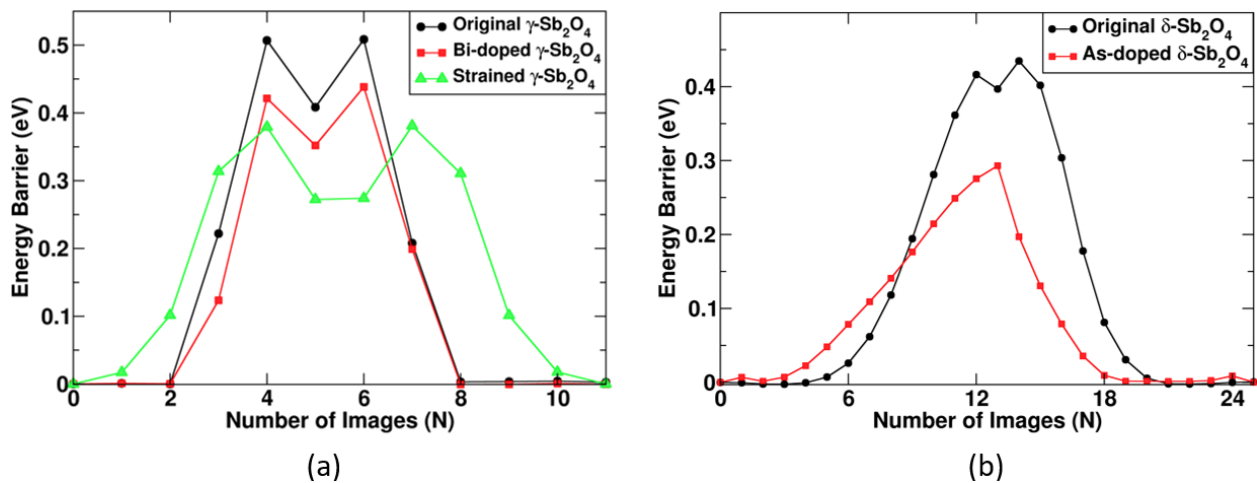


Figure 2: Switching energy barriers of (a) bulk γ - Sb_2O_4 and (b) bulk δ - Sb_2O_4 phases using the solid-state NEB method. The slight asymmetry is due to the influence of stacking.

The structural anisotropy in the Sb_2O_4 phases enables them to possess interesting properties, including ferroelectricity which arises from the breaking of the 180° inversion symmetry in-plane (δ phase) and out-of-the plane (γ phase). Further, the variability of Sb-O bonds arising from the lattice distortion results in the double- and single-well soft mode potentials in γ - and δ - phase, resembling some of the previously studied ferroelectrics^{6,11,13}. In SbSI, a well-known Sb-based ferroelectric material investigated several decades ago, and the ferroelectric behavior is associated with thermal fluctuations, change in electronic structure, atomic disorder, and phonon interactions,³⁶ all closely related to the variability of bonding between Sb and S/I. The finding of 2D ferroelectric Sb_2O_4 is another manifestation of the rich behavior of Sb-based compounds and its potential for future discoveries. As we will discuss below, the Sb-O system further provides an avenue for ferroelectrics with large band gaps, which are beneficial for the applications.

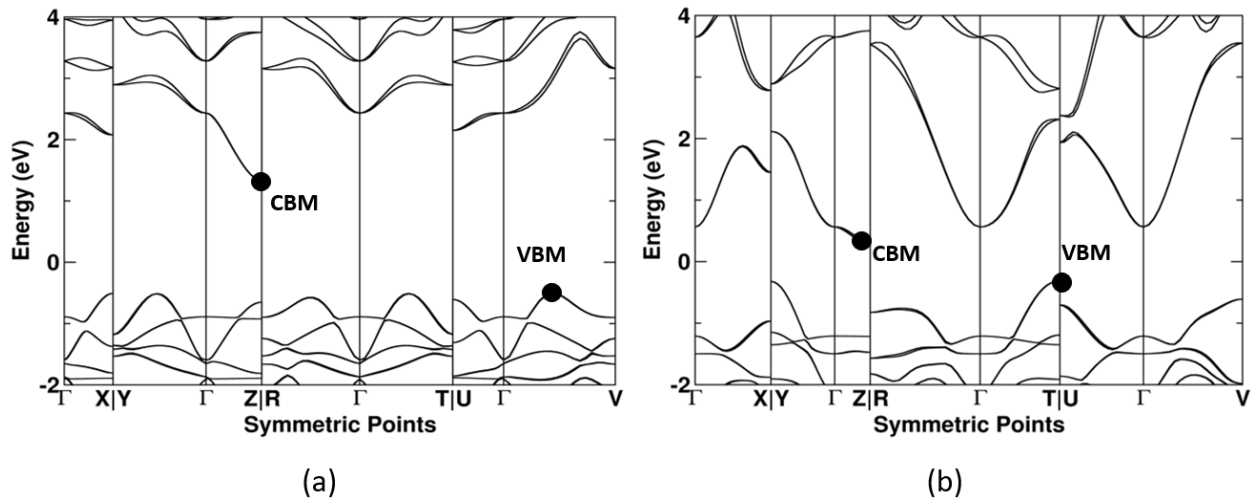


Figure 3: Band structures of (a) bulk γ - Sb_2O_4 , and (b) bulk δ - Sb_2O_4 using DFT method considering the spin orbit interaction.

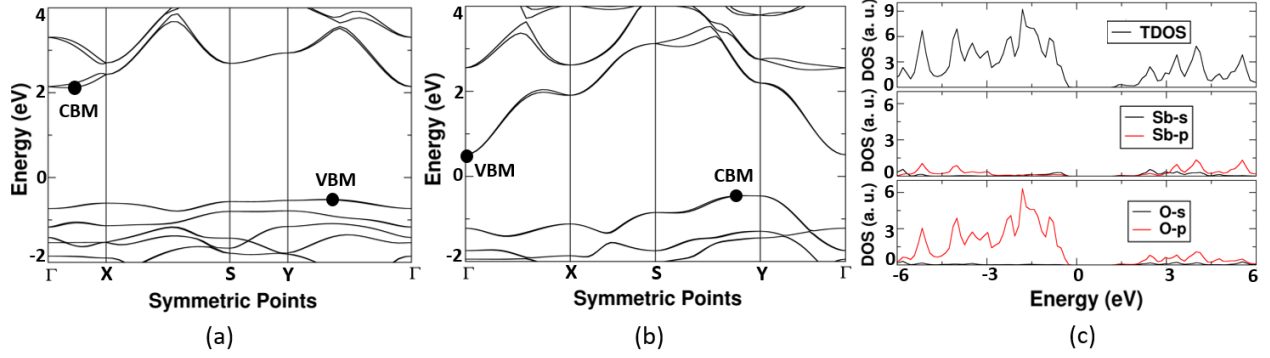


Figure 4: (a, b) DFT band structures of γ -Sb₂O₄, and δ -Sb₂O₄ monolayers (c) density of states of bulk γ -Sb₂O₄. Spin-orbit interaction is considered into account.

The electronic band structures of γ -Sb₂O₄ and δ -Sb₂O₄ using the standard DFT method are shown in Figure 3. The spin-orbit effects are considered in the calculations. In the bulk γ -Sb₂O₄ (Fig. 3(a)), the maximum of the valence band (VBM) lies between the Γ and V points, whereas the minimum of the conduction band (CBM) lies at the Z point in the Brillouin zone, giving rise to an indirect band gap of 1.88 eV. In bulk δ -Sb₂O₄ (Fig. 3(b)), the VBM lies between Γ and Z (very close to Z), and CBM lies at T, giving rise to an indirect band gap of 0.63 eV. The band structures of corresponding monolayers are shown in Figs. 4(a) and 4(b). In γ -Sb₂O₄ monolayer, VBM and CBM are located between Γ & X and Γ & Y, which give rise to an indirect band gap of 2.63 eV, whereas in δ -Sb₂O₄ monolayer, they are located at G, and between S & Y, thus making an indirect band gap of 0.96 eV. We also calculated the density of states (DOS) in each configuration. The compositions of DOS are similar in all cases, and therefore only the DOS of γ -Sb₂O₄ is presented in Figure 4(c). The p-orbitals of Sb and O atoms are dominant in both the valence band and conduction band (with p-orbitals of O in higher magnitude), while contributions from the respective s-orbitals are negligible.

Table 2: Band gaps of γ -Sb₂O₄, and δ -Sb₂O₄ phases under different methods

Phase	DFT Band gap (eV)	HSE Band gap (eV)	GW Band gap (eV)
γ -Sb ₂ O ₄ (bulk)	1.84	2.99	3.66
γ -Sb ₂ O ₄ (monolayer)	2.63	3.85	5.51
δ -Sb ₂ O ₄ (bulk)	0.63	1.56	2.25
δ -Sb ₂ O ₄ (monolayer)	0.96	2.05	3.39

To get further insight into the electronic properties, we perform the Bader charge analysis in the bulk phases. In γ - Sb_2O_4 , each octahedrally bonded Sb atom loses a charge of 2.66e (e being the electron charge of -1.67×10^{-19} C) to oxygen, whereas each tetrahedrally bonded Sb atom loses relatively less charge (1.83e). Each two-fold coordinated oxygen receives a charge of 1.11e, whereas each three-fold coordinated oxygen receives a slight more charge of 1.14e. In δ - Sb_2O_4 , the corresponding values are 2.28e & 1.81e for Sb atoms, and 1.13e & 1.15e for the oxygen atoms. This charge transfer mechanism is consistent with the fact that the oxygen is more electronegative than the antimony atom.

As DFT is known to underestimate the band gap, we perform the hybrid DFT (HSE) calculation (including spin-orbit interaction) to better approximate the gap values.³⁷⁻³⁹ We find the corresponding band gaps as 2.99 and 3.85 eV for the bulk and monolayer γ - Sb_2O_4 , 2.05 and 1.56 eV for the bulk and monolayer δ - Sb_2O_4 , respectively. To further improve the prediction of the band gaps of these phases, we employ the GW method⁴⁰⁻⁴² on top of DFT to include the quasiparticles effect. As the convergence under the GW method requires a sufficiently large number of empty conduction bands, we include 60 (17 of them are occupied) bands in our calculations, making sure that the supplied empty bands are sufficient for accurate results. From the GW approximation, the QP effect increases the band gaps to 3.66 eV, 5.55 eV, 2.25 eV, and 3.39 eV for bulk γ - Sb_2O_4 , monolayer γ - Sb_2O_4 , bulk δ - Sb_2O_4 , and monolayer δ - Sb_2O_4 , respectively (see Table 2). The large band gap values, especially in γ - and δ - Sb_2O_4 monolayers, are beneficial for their potential applications as a ferroelectric material in electronic devices.

Raman spectroscopy is a widely used technique to characterize materials. To facilitate the experimental exploration of the predicted Sb_2O_4 structures, we calculated the Raman spectra as shown in Figure 5 for the bulk and monolayers. In the bulk γ - Sb_2O_4 (Fig. 5(a)), two major Raman peaks are observed at 525 and 583 cm^{-1} , whereas in the monolayer (Fig. 5(b)), four peaks are observed at 444, 558, 610, and 699 cm^{-1} . Two major Raman peaks are observed at 511 and 635 cm^{-1} in bulk δ - Sb_2O_4 (Fig. 5(c)) and 378 and 526 cm^{-1} in the monolayer (Fig. 5(d)). In addition to the major peaks, some minor Raman peaks are also shown in the spectra. The detailed tabulation of the vibration modes is shown in Supplementary Information, Section IV. In addition to the Raman spectra, we also present the simulated XRD results using Cu-k alpha method in Supplementary Information, Section V to further assist experiments.

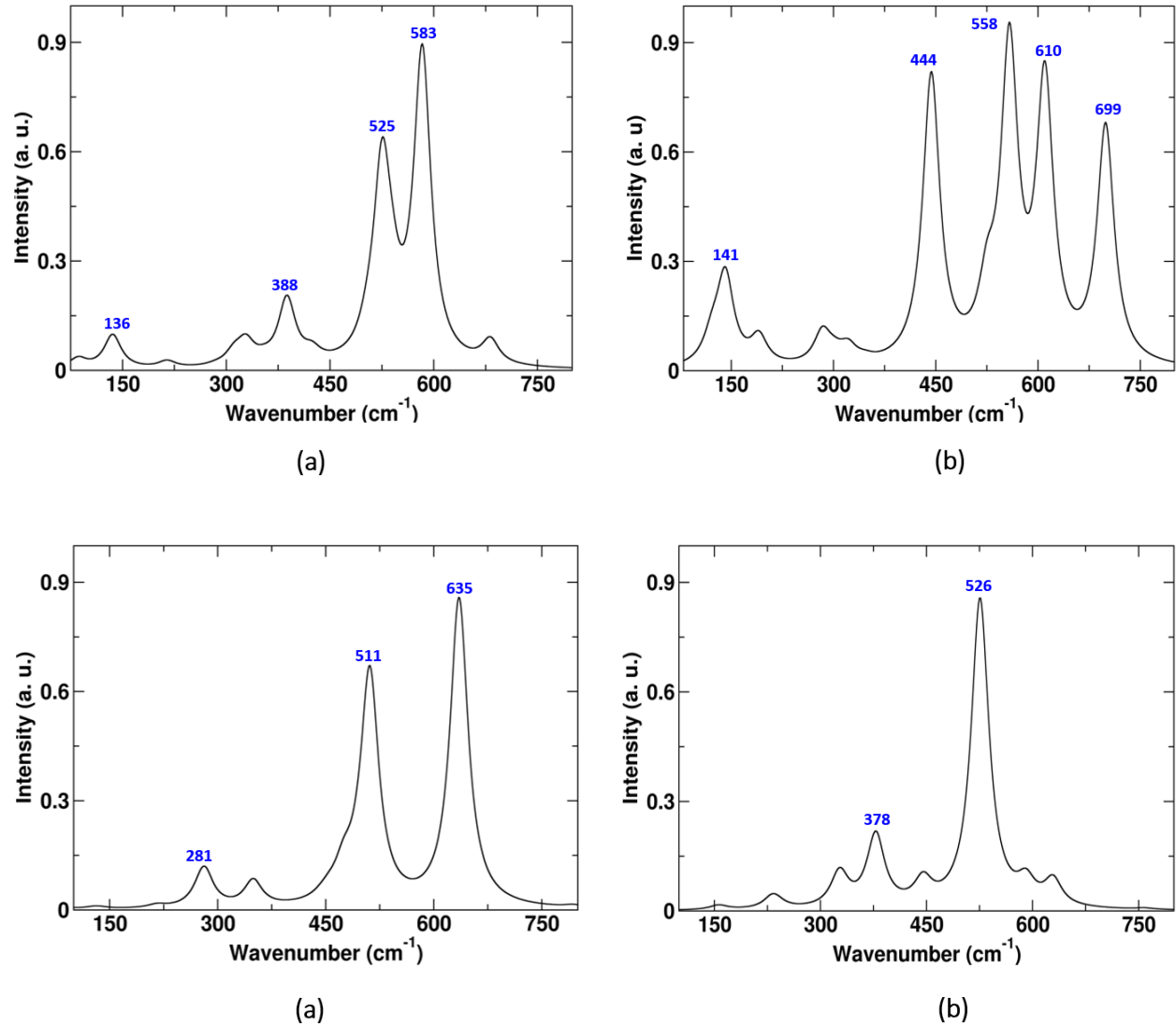


Figure 5: Calculated Raman spectra of (a) bulk γ -Sb₂O₄, (b) γ -Sb₂O₄ monolayer, (c) bulk δ -Sb₂O₄, and (d) δ -Sb₂O₄ monolayer.

Conclusions

Using the evolutionary algorithm combined with the first-principles DFT calculations, we predict the first two-dimensional (2D) polymorphs of antimony dioxide, namely, γ -Sb₂O₄ and δ -Sb₂O₄. Out-of-plane ferroelectricity is found in γ -Sb₂O₄, while in-plane ferroelectricity is found in δ -Sb₂O₄. We also show that doping with other group V elements or applying strain can lower the switching energy barriers. The dipole moment of γ -Sb₂O₄ and δ -Sb₂O₄ are calculated as 36.63 and 14.96 eÅ per unit cell, respectively, implying they are good candidates for ferroelectric applications. Furthermore, calculations show the indirect band

gaps of 5.51 and 3.39 eV for γ - and δ -Sb₂O₄ in their monolayers, respectively. Raman spectra are predicted to pave the way for the experimental investigation of the predicted structures. The existence of both in-plane and out-of-plane 2D ferroelectricity and the large band gap are notable features of these new phases, which may be of interest for potential applications.

Supplementary Material

Computational details, stability of γ - and δ -Sb₂O₄ monolayers including interlayer coupling energy, phonon spectra and AIMD graphs, detailed bonding analysis, vibrational modes, and simulated XRD spectra.

Acknowledgements

This work at the University of Memphis was supported by the National Science Foundation under Grant No. DMR 1709528 and by the Ralph E. Powe Jr. Faculty Enhancement Awards from Oak Ridge Associated Universities (ORAU). Computational resources were provided by the High-Performance Computing Center (HPCC) at the University of Memphis. It is also partially supported by the U.S. Department of Energy, Office of Science, Office of Basic Energy Sciences Energy Frontier Research Centers program under Award Number DESC0021118.

Competing Interests

The authors declare no competing financial interests.

Data Availability

The data that support the findings of this study are available from the corresponding author upon reasonable request.

References

1. Scott, J. F. Applications of Modern Ferroelectrics. *Science* **315**, 954–959 (2007).
2. Setter, N. *et al.* Ferroelectric thin films: Review of materials, properties, and applications. *J. Appl. Phys.* **100**, 051606 (2006).
3. Zhong, W., King-Smith, R. D. & Vanderbilt, D. Giant LO-TO splittings in perovskite ferroelectrics. *Phys. Rev. Lett.* **72**, 3618–3621 (1994).

4. Batra, I. P., Wurfel, P. & Silverman, B. D. New Type of First-Order Phase Transition in Ferroelectric Thin Films. *Phys. Rev. Lett.* **30**, 384–387 (1973).
5. Sharma, P. *et al.* A room-temperature ferroelectric semimetal. *Sci. Adv.* **5**, eaax5080 (2019).
6. Zhou, Y. *et al.* Out-of-Plane Piezoelectricity and Ferroelectricity in Layered α -In₂Se₃ Nanoflakes. *Nano Lett.* **17**, 5508–5513 (2017).
7. Chang, K. *et al.* Discovery of robust in-plane ferroelectricity in atomic-thick SnTe. *Science* **353**, 274–278 (2016).
8. Liu, F. *et al.* Room-temperature ferroelectricity in CuInP₂S₆ ultrathin flakes. *Nat. Commun.* **7**, 12357 (2016).
9. Fei, Z. *et al.* Ferroelectric switching of a two-dimensional metal. *Nature* **560**, 336–339 (2018).
10. Gao, Y., Wu, M. & Cheng Zeng, X. Phase transitions and ferroelasticity–multiferroicity in bulk and two-dimensional silver and copper monohalides. *Nanoscale Horiz.* **4**, 1106–1112 (2019).
11. Wu, M. & Zeng, X. C. Intrinsic Ferroelasticity and/or Multiferroicity in Two-Dimensional Phosphorene and Phosphorene Analogues. *Nano Lett.* **16**, 3236–3241 (2016).
12. Ding, W. *et al.* Prediction of intrinsic two-dimensional ferroelectrics in In₂Se₃ and other III₂-VI₃ van der Waals materials. *Nat. Commun.* **8**, 14956 (2017).
13. Gao, W. & Chelikowsky, J. R. Prediction of Intrinsic Ferroelectricity and Large Piezoelectricity in Monolayer Arsenic Chalcogenides. *Nano Lett.* **20**, 8346–8352 (2020).
14. Higashitarumizu, N. *et al.* Purely in-plane ferroelectricity in monolayer SnS at room temperature. *Nat. Commun.* **11**, 2428 (2020).
15. Chang, K. *et al.* Microscopic Manipulation of Ferroelectric Domains in SnSe Monolayers at Room Temperature. *Nano Lett.* **20**, 6590–6597 (2020).
16. Wolff, S., Gillen, R., Assebban, M., Abellán, G. & Maultzsch, J. Two-Dimensional Antimony Oxide. *Phys. Rev. Lett.* **124**, 126101 (2020).
17. Messalea, K. A. *et al.* High-k 2D Sb₂O₃ Made Using a Substrate-Independent and Low-Temperature Liquid-Metal-Based Process. *ACS Nano* **15**, 16067–16075 (2021).

18. Yang, K. *et al.* Ultrathin high- κ antimony oxide single crystals. *Nat. Commun.* **11**, 2502 (2020).
19. Cody, C. A., DiCarlo, L. & Darlington, R. K. Vibrational and thermal study of antimony oxides. *Inorg. Chem.* **18**, 1572–1576 (1979).
20. Roberts, E. J. & Fenwick, F. THE ANTIMONY-ANTIMONY TRIOXIDE ELECTRODE AND ITS USE AS A MEASURE OF ACIDITY ¹. *J. Am. Chem. Soc.* **50**, 2125–2147 (1928).
21. Skapski, A. C. & Rogers, D. The structure of SbNbO₄, α -Sb₂O₄, and SbTaO₄. *Chem. Commun. Lond.* 611–613 (1965) doi:10.1039/C19650000611.
22. Stewart, D. J., Knop, O., Ayasse, C. & Woodhams, F. W. D. Pyrochlores. VII. The Oxides of Antimony: an X-Ray and Mössbauer Study. *Can. J. Chem.* **50**, 690–700 (1972).
23. Allen, J. P., Carey, J. J., Walsh, A., Scanlon, D. O. & Watson, G. W. Electronic Structures of Antimony Oxides. *J. Phys. Chem. C* **117**, 14759–14769 (2013).
24. Nilsson, J., Landa-Cánovas, A., Hansen, S. & Andersson, A. Catalysis and structure of the SbVO₄/Sb₂O₄ system for propane ammoxidation. *Catal. Today* **33**, 97–108 (1997).
25. Matsumura, H. *et al.* Selective oxidation of methane to formaldehyde over antimony oxide-loaded catalyst. *J. Mol. Catal. Chem.* **250**, 122–130 (2006).
26. Youk, J. H., Boulares, A., Kambour, R. P. & MacKnight, W. J. Polymerization of Ethylene Terephthalate Cyclic Oligomers with a Cyclic Dibutyltin Initiator [†]. *Macromolecules* **33**, 3600–3605 (2000).
27. Galip, H., Hasipoğlu, H. & Gündüz, G. Flame-retardant polyester. *J. Appl. Polym. Sci.* **74**, 2906–2910 (1999).
28. Weil, E. D., Levchik, S. & Moy, P. Flame and Smoke Retardants in Vinyl Chloride Polymers – Commercial Usage and Current Developments. *J. Fire Sci.* **24**, 211–236 (2006).
29. Brebu, M., Jakab, E. & Sakata, Y. Effect of flame retardants and Sb₂O₃ synergist on the thermal decomposition of high-impact polystyrene and on its debromination by ammonia treatment. *J. Anal. Appl. Pyrolysis* **79**, 346–352 (2007).

30. Zhang, S. *et al.* Antimonene Oxides: Emerging Tunable Direct Bandgap Semiconductor and Novel Topological Insulator. *Nano Lett.* **17**, 3434–3440 (2017).
31. Amoroso, D. & Picozzi, S. *Ab initio* approach to structural, electronic, and ferroelectric properties of antimony sulphoiodide. *Phys. Rev. B* **93**, 214106 (2016).
32. Fatuzzo, E. *et al.* Ferroelectricity in SbSI. *Phys. Rev.* **127**, 2036–2037 (1962).
33. Noor-A-Alam, M., Z. Olszewski, O. & Nolan, M. Ferroelectricity and Large Piezoelectric Response of AlN/ScN Superlattice. *ACS Appl. Mater. Interfaces* **11**, 20482–20490 (2019).
34. Song, S. *et al.* Ferroelectric polarization switching with a remarkably high activation energy in orthorhombic GaFeO₃ thin films. *NPG Asia Mater.* **8**, e242–e242 (2016).
35. Sante, D. D., Stroppa, A. & Picozzi, S. Structural, electronic and ferroelectric properties of croconic acid crystal: a DFT study. *Phys. Chem. Chem. Phys.* **14**, 14673–14681 (2012).
36. Audzijonis, A., Grigas, J., Kajokas, A., Kvedaravičius, S. & Paulikas, V. Origin of ferroelectricity in SbSI. *Ferroelectrics* **219**, 37–45 (1998).
37. Heyd, J. & Scuseria, G. E. Efficient hybrid density functional calculations in solids: Assessment of the Heyd–Scuseria–Ernzerhof screened Coulomb hybrid functional. *J. Chem. Phys.* **121**, 1187–1192 (2004).
38. Heyd, J., Scuseria, G. E. & Ernzerhof, M. Erratum: “Hybrid functionals based on a screened Coulomb potential” [*J. Chem. Phys.* 118, 8207 (2003)]. *J. Chem. Phys.* **124**, 219906 (2006).
39. Heyd, J., Scuseria, G. E. & Ernzerhof, M. Hybrid functionals based on a screened Coulomb potential. *J. Chem. Phys.* **118**, 8207–8215 (2003).
40. Hedin, L. New Method for Calculating the One-Particle Green’s Function with Application to the Electron-Gas Problem. *Phys. Rev.* **139**, A796–A823 (1965).
41. Hybertsen, M. S. & Louie, S. G. Electron correlation in semiconductors and insulators: Band gaps and quasiparticle energies. 24.
42. Onida, G., Reining, L. & Rubio, A. Electronic excitations: density-functional versus many-body Green’s-function approaches. *Rev. Mod. Phys.* **74**, 601–659 (2002).

Supplementary Material

Ferroelectric 2D Antimony Oxides with Wide Bandgaps

Romakanta Bhattarai^a, Kai Ni^b, and Xiao Shen^{a*}

^aDepartment of Physics and Materials Science, The University of Memphis, Memphis, TN, USA

^bDepartment of Electrical and Microelectronic Engineering, Rochester Institute of Technology, Rochester, NY, USA

*xshen1@memphis.edu

I. Computational Details

The computational study in this work is carried out as follows. First, we use the genetic algorithm in combination with the density functional theory (DFT) to search for stable structures corresponding to the local energy minimum. Initially, a set of 30 structures are generated randomly from the space group set, and this number is preserved in each generation afterward. The calculation is stopped when the most stable structure remains unchanged in the fifteen generations. The best candidates in every generation are used to produce the offspring for the next generation. Heredity accounts for half of the candidates in each generation. The remaining half is produced from the space group symmetry (20%), soft mutation (10%), lattice mutation (10%), and permutation (10%). During the search, the number of atoms are varied from 3 to 30 with the stoichiometry of Sb_2O_4 . The searches are carried out for both 3D and 2D dimensions. We use the USPEX^{1,2} code for the genetic algorithm and the VASP³ code for DFT calculations, with the Perdew-Burke-Ernzerhof (PBE)⁴ type of exchange and correlation functional and the projected augmented wave (PAW)⁵ type pseudopotential. The electronic and ionic convergence conditions are set to 10^{-5} and 10^{-4} eV, respectively, along with the plane-wave basis set having a maximum energy cutoff of 320 eV. The electric dipole moments in γ - Sb_2O_4 and δ - Sb_2O_4 phases are calculated using the Berry-phase method.^{6,7}

The most stable structures predicted from the USPEX are relaxed in a tighter convergence criterion. A plane-wave basis set with the energy cutoff of 500 eV, in addition to the thresholds of 10^{-9} eV and 10^{-4} eV/Å for the electronic energy and force convergence, are considered in these calculations. For the integration of the Brillouin zone, Γ -centered k-points grids of $15 \times 15 \times 15$ and $15 \times 15 \times 1$ are chosen for the bulk and the corresponding monolayers, respectively. The dynamical stability of the predicted structures is tested using their respective supercells implemented in the Phonopy package,⁸ which works under the finite displacement method. Furthermore, the thermal stability is confirmed by performing the ab initio molecular dynamics simulations at 500 K for 30 ps.

The energy barrier for switching is calculated using the solid-state nudged elastic band (SS-NEB) method.⁹ The convergence criterion is set such that the force between any two successive steps is less than 0.01 eV/Å. The Raman spectra of the predicted structures are calculated using the density functional perturbation theory as implemented in the Quantum Espresso package.¹⁰ Norm-conserving pseudopotentials generated via Rappe-Rabe-Kaxiras-Joannopoulos (RRKJ)¹¹ scheme along with the PBE functional is used. The energy cutoff for the plane-wave basis set is 80 Rydberg. The total energy convergence criteria are set to 10^{-12} , and 10^{-14} Ry, respectively, for the self-consistency and the phonon calculations.

II. Stability of γ - and δ -Sb₂O₄ Monolayers

We construct the monolayers of γ - and δ -Sb₂O₄ and test the dynamical stabilities. First, we calculate the interlayer coupling energies and plot them as functions of interlayer distances, as shown in Fig. S1. The plots confirm that the monolayers are energetically stable and indicate the possibility of experimental synthesis of these monolayers.

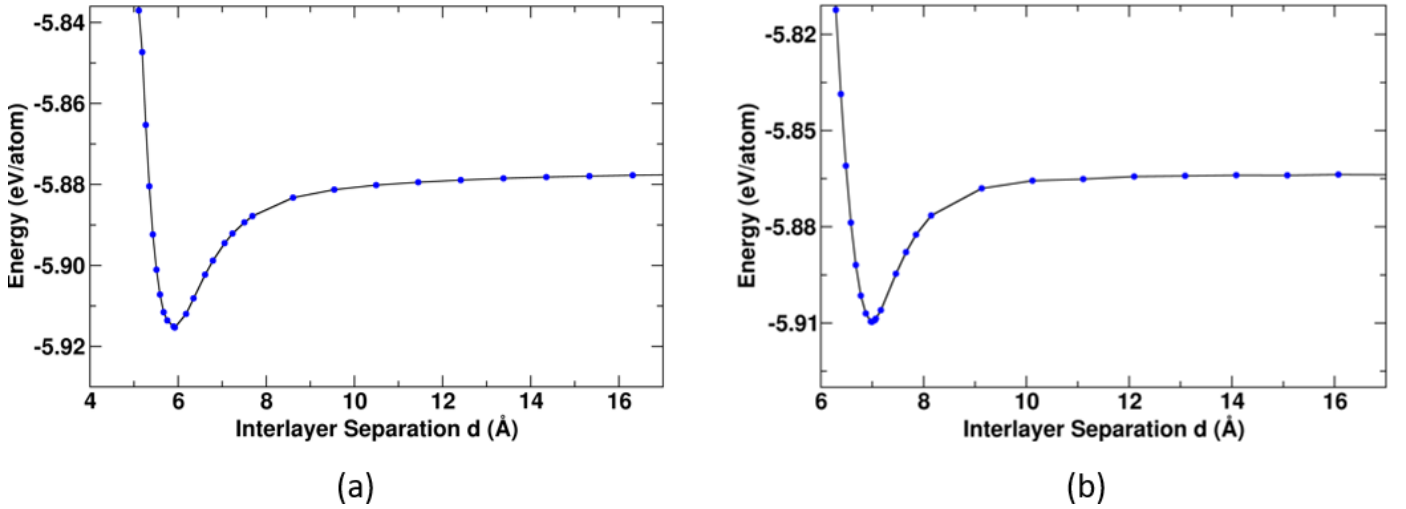


Figure S1: Coupling energy of as a function of interlayer separation (a) γ -Sb₂O₄, and (b) δ -Sb₂O₄

We then test the dynamical stability of all phases by calculating the phonon spectra using the Phonopy⁸ package. Since we have confirmed that the monolayer of γ - and δ -Sb₂O₄ are energetically stable, testing the dynamical stability of these monolayers should be sufficient for the dynamical stability of the corresponding bulk phases. Therefore, we present the phonon dispersion spectra of γ - and δ -Sb₂O₄ monolayers in Figs. S2(a), and S3(a), respectively. There are no sizable imaginary frequencies in the phonon spectra in any case, which indicates that the corresponding structures are dynamically stable. A very small imaginary frequency appears near the Γ point in the γ -Sb₂O₄ phase, which is because of the numerical artifacts in the calculations. This could be removed by using larger supercell sizes or

increasing the precisions (increased sampling points, larger energy cutoff, and tightening the criteria for electronic convergence).

In addition, we also test the thermal stability of the monolayers by performing the ab initio molecular dynamics (AIMD) simulation at an elevated temperature. The AIMD simulations are carried out in supercells of monolayers at 500 K for 30 ps with a time step of 2 fs. The potential energy profiles are plotted as a function of time, as shown in Figs. S2(b) and S3(b), for γ - and δ -Sb₂O₄ monolayers, respectively. Inserts represent the corresponding snapshots of the structures during the simulation. No sudden drop of the fluctuating potential energy, as well as no structure reconstruction throughout the simulation time, is observed, which implies the thermal stability of the structures.

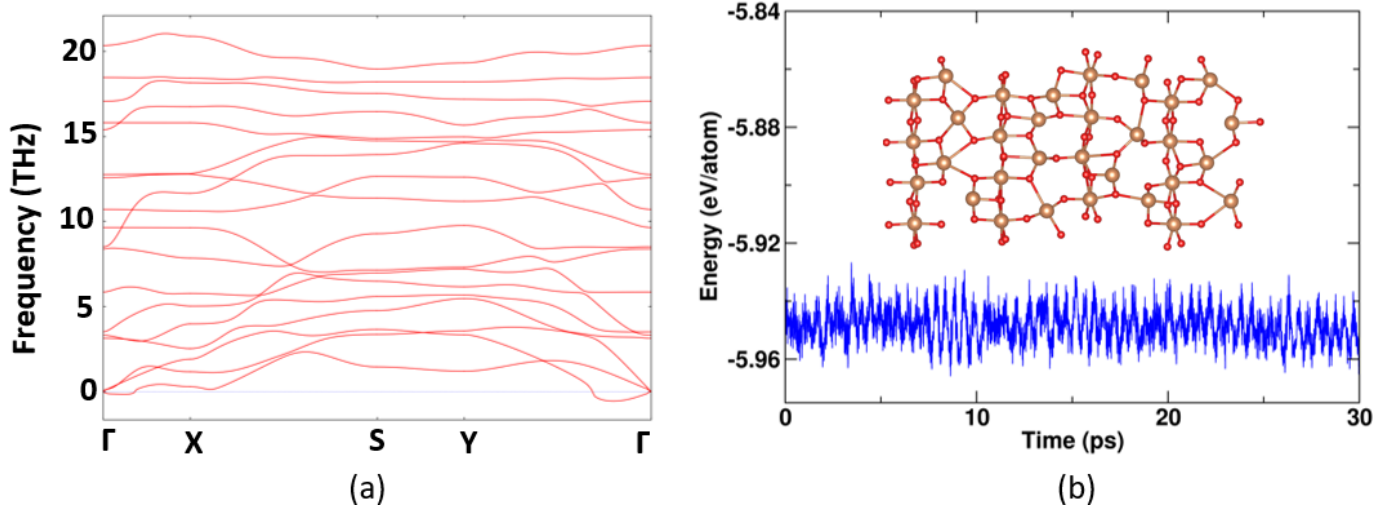


Figure S2: (a) Phonon band structures of monolayer γ -Sb₂O₄ (b) Potential energy profile of AIMD simulation of monolayer γ -Sb₂O₄ at 500 K for 30 ps. Insert shows a snapshot of structure during the simulation.

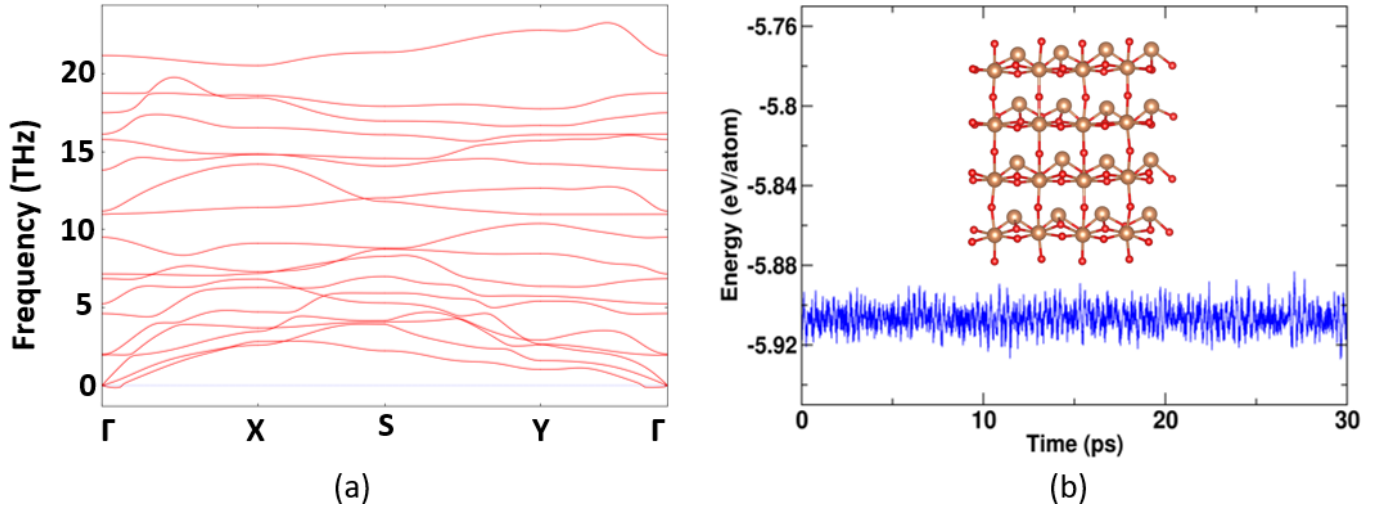


Figure S3: (a) Phonon band structures of monolayer δ -Sb₂O₄ (b) Potential energy profile of AIMD simulation of monolayer δ -Sb₂O₄ at 500 K for 30 ps. Insert shows a snapshot of structure during the simulation.

III. Bonding Analysis on γ - and δ -Sb₂O₄

To get a deeper insight into the bonding nature among γ - and δ -Sb₂O₄, we plot each phase separately, highlighting every Sb-O bond in Fig. S4. Each ion is labeled to facilitate comparison with the bond lengths in Table S1.

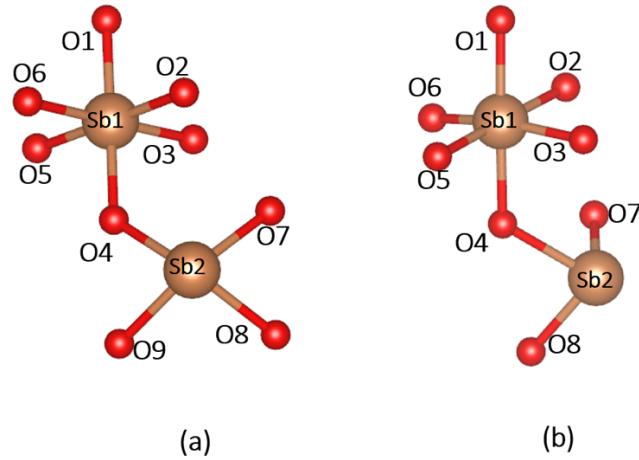


Figure S4: Bonding environments of Sb ions in (a) γ -Sb₂O₄, and (b) δ -Sb₂O₄

The structural configuration of γ -Sb₂O₄ looks similar to δ -Sb₂O₄; however, in reality, they differ in various aspects, including bond lengths, bond angles, et al., which give rise to separate properties between them.

Table S1 below compares the bonding environments between the two Sb₂O₄ structures.

Table S1: Comparison of bonding environments among γ -Sb₂O₄, and δ -Sb₂O₄

Phases	Bonding pairs	Bond lengths (Å)	Bonding pairs	Bond lengths (Å)
γ -Sb ₂ O ₄ (bulk)	Sb1-O1	2.067	Sb2-O4	2.153
	Sb1-O2	2.012	Sb2-O7	2.159
	Sb1-O3	2.028	Sb2-O8	2.148
	Sb1-O4	2.054	Sb2-O9	2.157
	Sb1-O5	2.027		
	Sb1-O6	2.012		
γ -Sb ₂ O ₄ (monolayer)	Sb1-O1	2.116	Sb2-O4	2.159
	Sb1-O2	2.038	Sb2-O7	2.159
	Sb1-O3	1.991	Sb2-O8	2.128
	Sb1-O4	2.055	Sb2-O9	2.128
	Sb1-O5	1.991		
	Sb1-O6	2.038		
δ -Sb ₂ O ₄ (bulk)	Sb1-O1	2.051	Sb2-O4	2.213
	Sb1-O2	2.080	Sb2-O7	2.019
	Sb1-O3	1.966	Sb2-O8	2.019
	Sb1-O4	2.080		
	Sb1-O5	1.051		
	Sb1-O6	1.957		
δ -Sb ₂ O ₄ (monolayer)	Sb1-O1	1.992	Sb2-O4	2.070
	Sb1-O2	2.137	Sb2-O7	2.025
	Sb1-O3	2.001	Sb2-O8	2.025
	Sb1-O4	2.138		
	Sb1-O5	1.992		
	Sb1-O6	1.993		

IV. Vibrational Modes

Both γ -Sb₂O₄ and δ -Sb₂O₄ have eighteen vibrational modes, as each unit cell contains six atoms in both phases. We tabulate the frequencies of these modes in Table S2, followed by plotting the vibrational eigenvectors in their bulk phases. We believe the results can be helpful for searching for these phases experimentally.

Table S2: Raman modes and corresponding vibrational frequencies of γ -Sb₂O₄, and δ -Sb₂O₄

Mode	γ -Sb ₂ O ₄ bulk	γ -Sb ₂ O ₄ monolayer	δ -Sb ₂ O ₄ bulk	δ -Sb ₂ O ₄ monolayer
------	---	--	---	--

	(cm ⁻¹)	(cm ⁻¹)	(cm ⁻¹)	(cm ⁻¹)
1	0	0	0	0
2	0	0	0	0
3	0	0	0	0
4	42	107	87	63
5	86	122	96	67
6	136	141	128	155
7	214	191	137	162
8	284	284	216	232
9	311	301	273	240
10	328	321	281	327
11	354	346	349	370
12	388	427	442	378
13	424	444	454	445
14	505	525	475	526
15	525	525	495	542
16	539	558	511	591
17	583	610	635	629
18	682	699	794	758

The first three modes in each phase having zero vibrational frequency represent the collective translational motion of the crystal units in the same direction (see below). The corresponding vibrational modes are presented in Figures S5 and S6. The antimony and oxygen atoms are represented by gray and red colors, respectively. The directions of displacements are shown by green arrows.

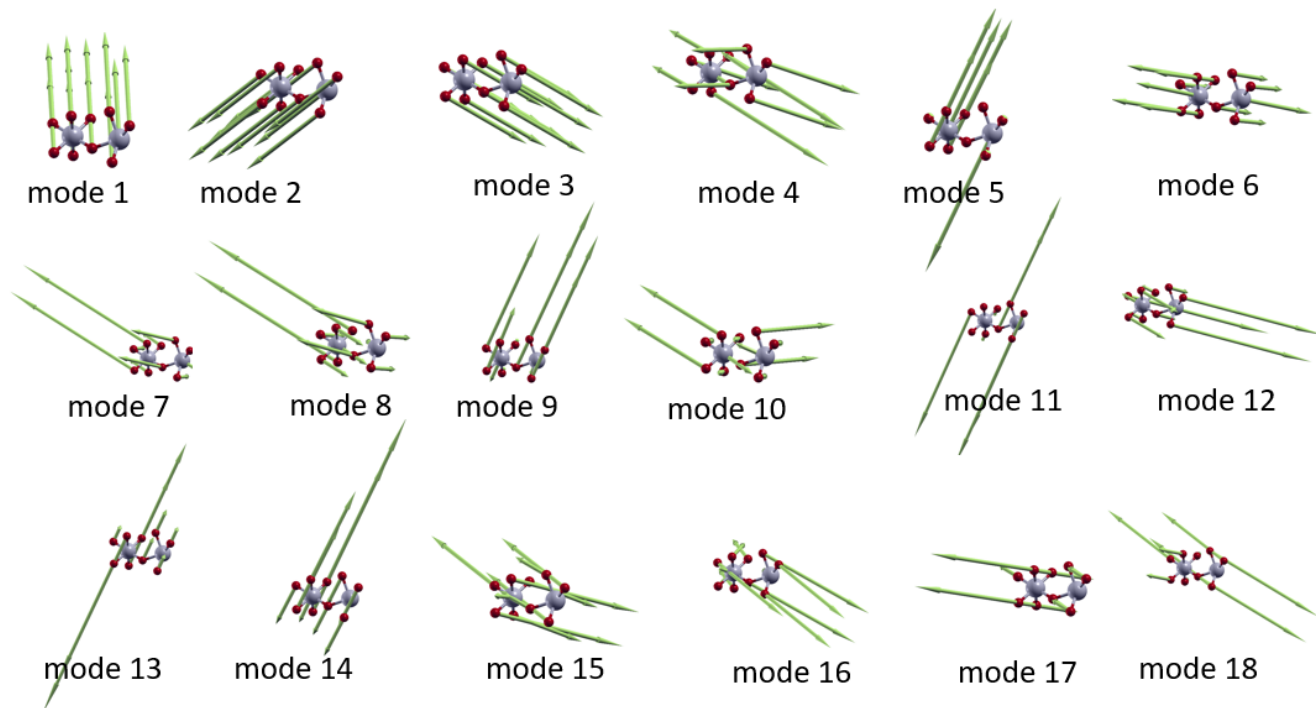


Figure S5: Eighteen vibrational modes of bulk γ - Sb_2O_4 .

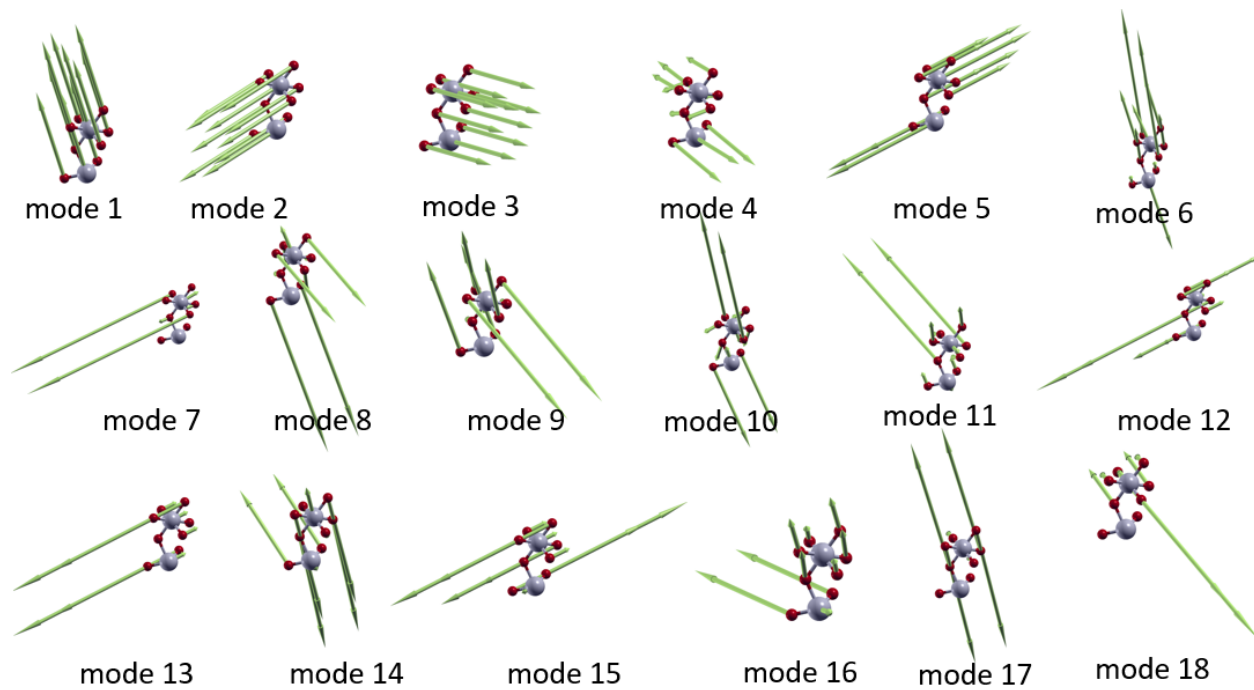


Figure S6: Eighteen vibrational modes of bulk δ - Sb_2O_4 .

V. X-Ray Diffraction (XRD) Spectra

In addition to Raman spectra, we also present the simulated XRD results using Cu-k alpha method in Table S3 below to further help the experimental investigations.

Table S3: Simulated XRD results of bulk γ -Sb₂O₄, and δ -Sb₂O₄ using Cu-k alpha method

S. N.	γ -Sb ₂ O ₄ 2 θ (°)	δ -Sb ₂ O ₄ 2 θ (°)
1	15.852	23.499
2	16.571	24.179
3	18.160	26.136
4	27.040	29.456
5	30.019	30.951
6	31.202	36.848
7	32.171	37.303
8	33.501	38.655
9	36.839	39.351
10	37.499	41.070
11	40.404	46.826
12	47.924	49.224
13	48.491	50.768
14	49.261	53.763
15	50.087	55.432
16	51.112	56.536
17	53.938	57.813
18	55.800	59.478
19	60.314	63.516
20	62.029	64.505
21	67.293	68.524

The XRD data are then plotted by showing the corresponding miller indices (hkl) in Figure S7 below.

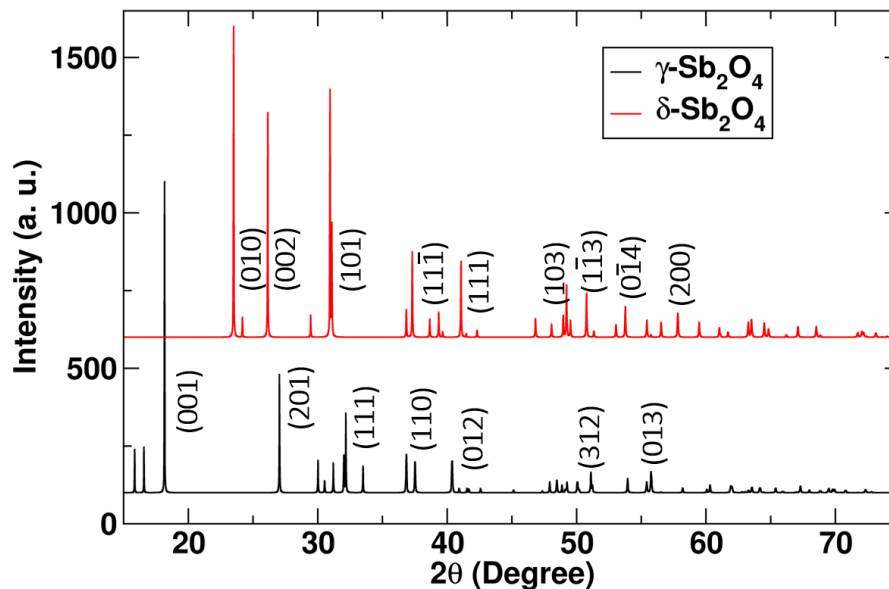


Figure S7: Plot of simulated XRD spectra of bulk $\gamma\text{-Sb}_2\text{O}_4$, and $\delta\text{-Sb}_2\text{O}_4$ using Cu-k alpha method

References:

1. Oganov, A. R., Lyakhov, A. O. & Valle, M. How Evolutionary Crystal Structure Prediction Works—and Why. *Acc. Chem. Res.* **44**, 227–237 (2011).
2. Lyakhov, A. O., Oganov, A. R., Stokes, H. T. & Zhu, Q. New developments in evolutionary structure prediction algorithm USPEX. *Comput. Phys. Commun.* **184**, 1172–1182 (2013).
3. Kresse, G. & Furthmüller, J. Efficient iterative schemes for ab initio total-energy calculations using a plane-wave basis set. *Phys. Rev. B* **54**, 11169–11186 (1996).
4. Perdew, J. P., Burke, K. & Ernzerhof, M. Generalized Gradient Approximation Made Simple. *Phys. Rev. Lett.* **77**, 3865–3868 (1996).
5. Blöchl, P. E. Projector augmented-wave method. *Phys. Rev. B* **50**, 17953–17979 (1994).
6. King-Smith, R. D. & Vanderbilt, D. Theory of polarization of crystalline solids. *Phys. Rev. B* **47**, 1651–1654 (1993).
7. Vanderbilt, D. & King-Smith, R. D. Electric polarization as a bulk quantity and its relation to surface charge. *Phys. Rev. B* **48**, 4442–4455 (1993).

8. Togo, A. & Tanaka, I. First principles phonon calculations in materials science. *Scr. Mater.* **108**, 1–5 (2015).
9. Sheppard, D., Xiao, P., Chemelewski, W., Johnson, D. D. & Henkelman, G. A generalized solid-state nudged elastic band method. *J. Chem. Phys.* **136**, 074103 (2012).
10. Giannozzi, P. *et al.* QUANTUM ESPRESSO: a modular and open-source software project for quantum simulations of materials. *J. Phys. Condens. Matter* **21**, 395502 (2009).
11. Rappe, A. M., Rabe, K. M., Kaxiras, E. & Joannopoulos, J. D. Optimized pseudopotentials. *Phys. Rev. B* **41**, 1227–1230 (1990).